CrossMark

Impact of Cosmic Rays on Atmospheric Ion Chemistry and Spectral Transmission Features of TRAPPIST-1e

Konstantin Herbst[1] , Andreas Bartenschlager[2] , John Lee Grenfell[3] , Nicolas Iro[3] , Miriam Sinnhuber[2] ,
Benjamin Taysum[3] , Fabian Wunderlich[3] , N. Eugene Engelbrecht[4] , Juandre Light[4,5] , Katlego D. Moloto[4] ,
Jan-Vincent Harre[3] , Heike Rauer[3,6] , and Franz Schreier[7]
[1] Institut für Experimentelle und Angewandte Physik, Christian-Albrechts-Universität zu Kiel, D-24118 Kiel, Germany; herbst@physik.uni-kiel.de
[2] Institut für Meteorologie und Klimaforschung, Karlsruher Institut für Technologie, D-76344 Eggenstein-Leopoldshafen, Germany
[3] Institut für Planetenforschung, Deutsches Zentrum für Luft- und Raumfahrt (DLR), D-12489 Berlin, Germany
[4] Centre for Space Research, North-West University, 2520, Potchefstroom, South Africa
[5] South African National Space Agency, Hermanus, South Africa
[6] Institut für Geologische Wissenschaften, Freie Universität Berlin, D-12249 Berlin, Germany
[7] Institut für Methodik der Fernerkundung, Deutsches Zentrum für Luft- und Raumfahrt (DLR), D-82234 Oberpfaffenhofen, Germany
Received 2023 May 26; revised 2023 October 16; accepted 2023 October 30; published 2024 January 23

Abstract

Ongoing observing projects like the James Webb Space Telescope and future missions offer the chance to characterize Earth-like exoplanetary atmospheres. Thereby, M dwarfs are preferred targets for transit observations, for example, due to their favorable planet–star contrast ratio. However, the radiation and particle environment of these cool stars could be far more extreme than what we know from the Sun. Thus, knowing the stellar radiation and particle environment and its possible influence on detectable biosignatures—in particular, signs of life like ozone and methane—is crucial to understanding upcoming transit spectra. In this study, with the help of our unique model suite INCREASE, we investigate the impact of a strong stellar energetic particle event on the atmospheric ionization, neutral and ion chemistry, and atmospheric biosignatures of TRAPPIST-1e. Therefore, transit spectra for six scenarios are simulated. We find that a Carrington-like event drastically increases atmospheric ionization and induces substantial changes in ion chemistry and spectral transmission features: all scenarios show high event-induced amounts of nitrogen dioxide (i.e., at 6.2 μm), a reduction of the atmospheric transit depth in all water bands (i.e., at 5.5–7.0 μm), a decrease of the methane bands (i.e., at 3.0–3.5 μm), and depletion of ozone (i.e., at ∼9.6 μm). Therefore, it is essential to include high-energy particle effects to correctly assign biosignature signals from, e.g., ozone and methane. We further show that the nitric acid feature at 11.0–12.0 μm, discussed as a proxy for stellar particle contamination, is absent in wet-dead atmospheres.

Unified Astronomy Thesaurus concepts: Biosignatures (2018); Exoplanet atmospheric composition (2021); Extrasolar rocky planets (511); Cosmic rays (329)

1. Introduction

More than 5500 exoplanets in over 4100 exoplanetary systems[8] have been detected since the discovery of the first Jupiter-mass exoplanet around a Sun-like star in 1995 (Mayor & Queloz 1995), ranging from hot gas giants to rocky Earth-like exoplanets around much smaller and cooler stars (i.e., M dwarfs). According to Hill et al. (2023), as of today, 17 of the rocky exoplanets with radii up to 1.6 $R_\oplus$, or masses up to 3 $M_\oplus$, are believed to lie in the conservative habitable zone (HZ), a region around the star determined by the runaway greenhouse in which the stellar radiation from one or multiple host stars allows for liquid water to exist for geological periods on the surface of the orbiting rocky exoplanets (e.g., Kasting et al. 1993).

Within the next decade, next-generation telescopes will provide new opportunities to study the atmospheres of Earth-like exoplanets. Currently, M dwarfs (making up to 75% of all stars in the solar neighborhood) in particular are favored targets for transit observations, due to their favorable planet–star contrast ratio and shorter orbital periods (more transit events over a given time).

Currently, one of the most exciting systems is that of TRAPPIST-1. The nearby ultracool M dwarf has several Earth-sized exoplanets, three of which, i.e., planets e (at 0.028 au), f (at 0.038 au), and g (at 0.047 au), are assumed to lie within the conservative stellar HZ (Hill et al. 2023), and thus may have equilibrium temperatures that support liquid surface water, one of the key ingredients for life as we know it from Earth. The first James Webb Space Telescope (JWST) observations of TRAPPIST-1b showed no atmospheric absorption of any species (Greene et al. 2023; Ih et al. 2023), while, with the help of JWST/NIRISS/SOSS transmission spectra, Lim et al. (2023) found strong stellar contamination in the order of hundreds of ppm and ruled out H$_2$-rich atmospheres. Thus, distinguishing between TRAPPIST-1b being a bare rock and/ or having a thin atmosphere is currently impossible. As discussed by Zieba et al. (2023), a thin, O$_2$-dominated, low-CO$_2$ atmosphere or a bare rock surface are possible explanations for the secondary eclipse depth of 421 ± 94 ppm at 15 μm that was revealed by the first JWST observations of TRAPPIST-1 c. Most recently, however, Lincowski et al. (2023) showed that steam atmospheres of $\geqslant 0.1$ bar and (although less likely) thick O$_2$-dominated atmospheres are also

---
[8] See, e.g., https://exoplanets.nasa.gov, last visited on 2023 October 13.

consistent with the observations. Nevertheless, our current knowledge of the TRAPPIST-1 system and its evolution does not rule out the possibility of Earth-like atmospheres on the planets further out in the system, in particular those within the HZ (see, e.g., discussion in Krissansen-Totton 2023).

Nevertheless, TRAPPIST-1 is known to be an active star with frequent (high-energy) stellar flaring (e.g., Vida et al. 2017) and EUV/XUV activity (Wheatley et al. 2017), which could strip away the planetary atmosphere and impact its habitability (e.g., Bourrier et al. 2017) by, e.g., reducing the chances for life to develop and persist on the planets within the HZ. As shown by, e.g., Herbst et al. (2019), Scheucher et al. (2020a), and Barth et al. (2021) in particular, cosmic rays of galactic and stellar origin play a crucial role in determining the atmospheric climate and chemistry and habitability on (Earth-like) exoplanets. Consistent studies on the impact of cosmic rays, however, are missing.

Thus, at the dawn of the age of atmospheric characterization of such Earth-like exoplanets with JWST, it is of utmost importance to study the atmospheric response to the stellar particle and radiation environment as preparation for interpreting the observations soon to come. By utilizing the INCREASE model suite, we—for the first time—will shed light on the impact of cosmic ray effects on the ion chemistry of a potentially Earth-like TRAPPIST-1e atmosphere.

2. Scientific Background

2.1. The Galactic Cosmic Ray Background

The transport of galactic cosmic rays (GCRs) within stellar astrospheres depends on different factors, such as the stellar type of the host star, its rotation rate, the stellar wind dynamics, and the stellar activity. Thereby, the stellar magnetic field defines the inner boundary conditions, while the local interstellar spectrum (LIS) forms the outer boundary condition. Initial model studies by Herbst et al. (2020a) have shown that cool star astrospheres may be rather diverse.

Based on our heliospheric knowledge, the modulation of GCRs within cool star astrospheres is usually based on solving the transport equation of Parker (1965), either analytically with the help of the force field solution (FFS; Gleeson & Axford 1968) or numerically by, e.g., employing stochastic differential equations (SDEs; see Strauss & Effenberger 2017; Moloto et al. 2019, and references therein).

However, little is known about the astrospheric environments of cool stars. Thus, either a modified FFS (e.g., Mesquita et al. 2021; Rodgers-Lee et al. 2021) or a 1D version of the transport equation is used to solve the transport of GCRs within astrospheres (e.g., Herbst et al. 2020b; Mesquita et al. 2022). By employing results from astrospheric 3D MHD modeling, Herbst et al. (2020b) suggested for the first time significant differences between the analytic and numerical solution, emphasizing that the GCR flux, in particular for cool star astrospheres, might have a much more significant impact on exoplanetary atmospheres, and thus their habitability, than previously thought. This is not unexpected, given the limitations implicit to the analytical force field and convection–diffusion approaches to solving Parker's transport equation (TPE; see, e.g., Caballero-Lopez & Moraal 2004; Caballero-Lopez et al. 2019; Engelbrecht & Di Felice 2020). Herbst et al. (2020b) further concluded that 3D transport modeling is mandatory in order to properly describe the GCR

transport—which, however, is difficult given the relatively unknown behavior of the astrospheric plasma environments (see also Light et al. 2022). More information on the importance of turbulence in astrospheres, known to be essential in modeling GCR transport from first principles (see also Engelbrecht et al. 2022), is discussed in Herbst et al. (2022b). Here, we solve the 1D Parker transport equation following the SDE approach outlined by Engelbrecht & Di Felice (2020) and Light et al. (2022), where

$$\frac{\partial f}{\partial t} = \frac{1}{r^2}\frac{\partial}{\partial r}\left(r^2\kappa_{rr}\frac{\partial f}{\partial r}\right) + \frac{1}{3r^2}\frac{\partial}{\partial r}(r^2V_s)\frac{1}{p^2}\frac{\partial}{\partial p}(p^3f)$$
$$- \frac{1}{r^2}\frac{\partial}{\partial r}(r^2V_sf), \tag{1}$$

expressed in terms of the omnidirectional GCR distribution function f, which is related via the momentum p to differential intensity by $f(r, p, t) = p^{-2}j_T$ (see, e.g., Moraal 2013). The above equation models GCR adiabatic energy changes, convection via the stellar wind speed V_s, and radial diffusion, controlled by the diffusion coefficient κ_{rr}. This quantity is modeled using the approach of Light et al. (2022), which employs an essentially Bohm diffusion coefficient in terms of its magnetic field dependence (see, e.g., Shalchi 2009), but modified with the rigidity dependence expected of a perpendicular diffusion coefficient derived using the nonlinear guiding center theory of Matthaeus et al. (2003), given by

$$\kappa_{rr} = \frac{v}{3}\lambda_0\left(\frac{B_0}{B}\right)\left(\frac{P}{P_0}\right)^{2/3}, \tag{2}$$

with P being the particle rigidity, and $P_0 = 1$ GV. The astrospheric magnetic field (AMF) is denoted by B and normalized to a value of B_0 at a distance $r_0 = 1$ au. The mean free path is scaled with the parameter $\lambda_0 = 0.01$ au to a value at r_0 within the range of what is expected from heliospheric modulation studies (see, e.g., Engelbrecht et al. 2022, and references therein).

Several assumptions must be made to model the large-scale plasma quantities required to solve the Parker TPE. First, it is assumed that the AMF of TRAPPIST-1 can be described using a Parker (1958) magnetic field model, at least within its termination shock. This assumption is based on the typical behavior of MHD-simulated AMFs for this type of star in this region (see Herbst et al. 2022b). To calculate such a field magnitude, we assume a stellar rotation period of 3.3 days (Luger et al. 2017), a stellar wind velocity of 1400 km s^{-1} (Garraffo et al. 2017), and a stellar surface field of 600 G (Harbach et al. 2021 and references therein). Accordingly, we assume a value of 1.8 nT for the AMF magnitude at 1 au. Given that, to the best of our knowledge, no large-scale MHD simulations for the TRAPPIST-1 astrosphere have been published, it is not possible to employ an estimate for its termination shock location based on the limited studies available. Therefore, it is assumed here as a first approach that its termination shock is located at 76 au, following the results of Herbst et al. (2020b) for Proxima Centauri. Given that the mass-loss rate for TRAPPIST-1 is expected to be larger than that for Proxima Centauri (Garraffo et al. 2017), this estimate is probably too low and may need to be revisited when full large-scale MHD simulations for the astrosphere become available in the literature. Because such an analytical approach is
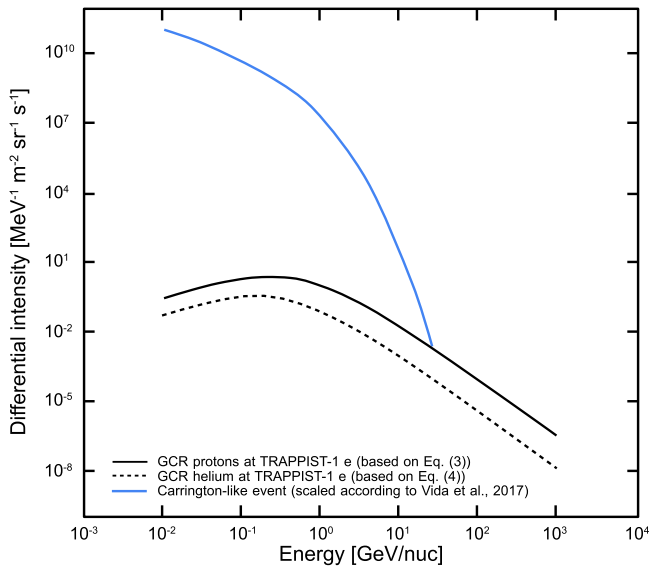
Figure 1. Differential primary GCR spectra for a quiescent TRAPPIST-1 (black lines) in comparison to a Carrington-like event scaled to the location of TRAPPIST-1e (see also Vida et al. 2017).

impossible for the astrosheath, we employ GCR proton and helium boundary spectra at this termination shock expression when we solve Equation (1). These are modeled following the approach of Engelbrecht & Moloto (2021), who fit spectral forms to Voyager observations for galactic cosmic ray intensities reported by Webber et al. (2008). For GCR protons, the boundary spectrum is given by

$$j_B(76 \text{ au}, \text{ H}) = \frac{17.0(P/P_o)^{-2.4}}{2.2 + 2.1(P/P_o)^{-3}}, \tag{3}$$

with units of particles $\text{m}^{-2} \text{ s}^{-1} \text{ sr}^{-1} \text{ MeV}^{-1}$, where P is in units of GV, and P_o is chosen to be equal to 1 GV. We note that here no time dependence is assumed for Equation (3), as was done by Engelbrecht & Moloto (2021).

The transport of helium within astrospheres has not previously been considered, even though it has been relatively well-studied in the heliospheric context (see, e.g., Shen et al. 2019). In this study, we assume the helium spectrum at 76 au to be given by

$$j_B(76 \text{ au}, \text{ He}) = \frac{3.3(P/P_o)^{-2.5}}{(1.2 + 5.0(P/P_o)^{-4.4})^{0.92}}, \tag{4}$$

constructed in the same manner as was Equation (3), and we will use the 1D SDE code at hand to study the modulation of these particles for the first time in an astrospheric context.

Although Equations (3) and (4) are strictly only applicable to heliospheric conditions, they nevertheless give an estimate of the modulation effects due to the astrosheath, in that they represent a considerable reduction of GCR intensities, as expected in the local interstellar medium (see, e.g., Herbst et al. 2017). This is because considerable GCR modulation has been reported in the heliosheath (e.g., Stone et al. 2013), and the same could be reasonably expected for astrospheres. The above expressions are shown, along with the calculated differential intensity spectra at the position of TRAPPIST-1e in Figure 1. Both spectra show a relatively low degree of modulation compared to Earth, with most modulation occurring at energies below ∼1 Gev/nucleon. This behavior is similar to that

reported by Herbst et al. (2020b) for Proxima Centauri b, resulting from the AMF dependence of the radial diffusion coefficient. At higher energies, the spectra remain almost unmodulated, as would be expected from the rigidity dependence of Equation (2).

2.2. The Stellar Particle Environment

One of the strongest solar flares ever observed in the heliosphere is the Carrington event, which occurred in September 1859. The corresponding flare was estimated to have had an energy of 10^{33} erg (Cliver et al. 2022) and resulted in one of the strongest geomagnetic storms ever impacting the Earth's atmosphere. Cosmogenic radionuclide records, in particular ^{10}Be, ^{14}C, and ^{36}Cl, however, suggest short-period increases in the production rates about 20 times larger than changes ascribed to solar modulation, indicating the existence of much more extreme events in the past (e.g., AD774/775; Miyake et al. 2012; Mekhaldi et al. 2015) that lead to extreme particle events strongly impacting the Earth's atmosphere. Unfortunately, information on the corresponding event spectra of historical events, such as the Carrington event, is lacking. For example, to this date, it is scientifically debated whether the corresponding production rate increases around AD774/775 were caused by a single extreme event or by multiple strong events within a short amount of time (e.g., Cliver et al. 2022; Papaioannou et al. 2023). Thus, historical events are usually scaled with the help of measured modern-era Ground Level Enhancement (GLE) events—strong solar energetic particle events that are detected by neutron monitors at the Earth's surface—on average occurring once every year.

Vida et al. (2017) analyzed the 80 day continuous short-cadence K2 observations of TRAPPIST-1 and revealed 42 flare events with integrated energies between 1.26×10^{30} and 1.24×10^{33} erg. Thus, Carrington-like events on TRAPPIST-1 occur frequently. As a first step, in this study, we investigate the impact of a single strong event. As suggested by Vida et al. (2017), therefore, the terrestrial Carrington event—based on the spectral shape of GLE44 (1989 October), with a rather flat spectrum but much higher intensities at lower energies—has been scaled to the location of TRAPPIST-1e (0.029 au) via $1/r^2$ (see blue line in Figure 1), which makes the Carrington-like event at TRAPPIST-1e more than 3 orders of magnitude stronger than the actual Carrington event that impacted the Earth. Further, we assume that particles—in principle—can be accelerated to higher energies during such strong flares, so we allowed particle energies up to 40 GeV. We note that, according to the flare frequency distribution (e.g., Vida et al. 2017; Glazier et al. 2020), TRAPPIST-1 is a constantly flaring star, indicating that Carrington-like flares could occur once every three months and that much stronger events could occur on an annual and decennial basis. Thus, the stellar activity of TRAPPIST-1 could constantly impact the atmospheres of its planets. In this study, we focus on the impact of a single Carrington-like event, while the impact of constant flaring will be discussed in a follow-up paper. Furthermore, we note that even stronger events (up to 6 orders of magnitude greater than current solar events, according to Fraschetti et al. 2019) might occur at TRAPPIST-1e, while it might also be possible that the stellar magnetic field of M dwarfs may prevent energetic particles from escaping during stellar flares and that corresponding CMEs may be confined (see Alvarado-Gómez et al. 2019; Fraschetti et al. 2019).

2.3. Cosmic-Ray-Induced Atmospheric Ion Pair Production

CRs entering a planetary atmosphere mainly lose their energy due to the ionization of ambient matter. Consequently, once the nucleonic-electromagnetic particle shower reaches the surface, the chances of it interacting with the surrounding gases (and the planetary surface) dramatically increase. Ionization of the lower and middle atmosphere occurs because of the production of charged secondary particles within the electromagnetic branch. The severity of this effect, however, varies considerably depending on several factors, including the energy of the primary particle, the type of the produced secondary particle, and the atmospheric depth (e.g., Banjac et al. 2019).

While the GCR-induced ionization is likely to be anticorrelated with the stellar activity (if present), a stellar energetic particle event can significantly contribute to atmospheric ionization only if very high-energy particles are produced in stellar flares and coronal mass ejections (CMEs).

The CR-induced ionization rate Q as a function of the stellar activity (via the stellar modulation parameter ϕ), cutoff energy (E_C), and the atmospheric altitude x numerically is described by

$$Q(\phi, E_C, x) = \sum_i \int_{E_{C,i}}^{\infty} J_i(\phi, E) \cdot Y_i(E, x) \, dE, \qquad (5)$$

where i represents the type of the primary cosmic ray particle (here protons and α-particles), $J_i(\phi, E)$ the primary differential energy spectrum of either GCRs or stellar energetic particles, and $Y_i(E, x)$ the atmospheric ionization yield.

The latter can be computed as

$$Y_i(E, x) = \alpha \cdot \frac{1}{E_{\mathrm{ion}}} \cdot \frac{\Delta E_i}{\Delta x}, \qquad (6)$$

and thus depends on the geometrical normalization factor $\alpha = 2\pi \int \cos(\theta) \sin\theta \, d\theta$, the depth-dependent mean specific energy loss $\frac{\Delta E_i}{\Delta x}$, and the atmospheric ionization energy E_{ion}. In all the investigated scenarios, Earth-like atmospheres—defined here as N_2–O_2–CO_2 dominated with 1–2 bar surface pressure (see Section 4.2)—are being studied. Therefore, an average ionization energy of 31.7 eV (see, e.g., Wedlund et al. 2011) is used, and an Earth-like magnetic field is assumed.

2.4. Cosmic-Ray-Induced Atmospheric Radiation Exposure

Besides atmospheric ionization profiles, the atmospheric radiation exposure can also be modeled with codes such as the Atmospheric Radiation Interaction Simulator (AtRIS; Banjac et al. 2019, see Section 3.1). As discussed in Herbst et al. (2020a), the precalculated relative ionization efficiency $\mathcal{I}_{R,j}$, given as $\mathcal{I}_{R,j}(E_i) := \frac{E_d}{E_i}$, with E_d representing the average ionization energy of a particle of type j is causing in a well-defined phantom like the phantom of the International Commission on Radiation Units and Measurement (ICRU; e.g., McNair 1981, mimicking the human body), is used. The average absorbed dose of the ICRU phantom is given as

$$\overline{D_j}(E_i, r) = \mathcal{I}_{R,j}(E_i) \cdot \frac{E_i}{m_{\mathrm{ph}}}, \qquad (7)$$

where E_i is the ionization energy and m_{ph} the mass of the phantom given by $\rho \cdot \frac{4}{3}\pi \cdot r_{\mathrm{ph}}^3$. Finally, the results are convoluted with the primary particle spectrum and summed up over all energy bins and particle types (i.e., protons and alphas).

2.5. Cosmic-Ray-Induced Ion Chemistry

Formation of NOx. The dissociation of N_2 by charged particle impact and fast ion chemistry reactions can lead to the production of NOx species (N, NO, and NO_2; see, e.g., Sinnhuber et al. 2012; Sinnhuber & Funke 2020 and references therein for recent reviews of the terrestrial atmosphere). While positively charged ions dominate in the lower thermosphere, negatively charged ions become more common in the layers below, affecting the partitioning and lifetime of NOx species. Recombination of NO^+ and N_2^+ with electrons is an important source of NOx. In addition, charge transfer of N^+ (Nicolet 1975) and ion–neutral reactions also contribute to the formation of NOx (Nicolet 1965). The nitrogen atoms formed by recombination can also occur in energetically different states. On the one hand, in the ground state $N(^4S)$, on the other hand, also in the excited states $N(^2D)$ and $N(^2P)$. They can react with O_2 and O_3 to form NO (Sinnhuber et al. 2012). The formation of nitrogen oxides NO and NO_2 as a consequence of particle precipitation is well known on Earth but has been found to depend on the large availability of N_2 as a nitrogen source. As nitrogen is one of the most abundant species in the CO_2-poor scenarios, large amounts of NOx are formed in quantities comparable to those of large particle events in the Earth's atmosphere (e.g., Jackman et al. 2000, 2001; Funke et al. 2011).

Production of HO_x and loss of water vapor. Water vapor is taken up into positive ions, forming large positive water cluster ions. In the process of water vapor uptake and in the recombination of the cluster ions with electrons or negative ions, H and OH are released into the gas phase. This process of HO_x formation was postulated for the first time based on observations of ozone loss by Swider & Keneshea (1973) and formulated concisely by Solomon et al. (1981). H and OH are released in equal parts, and this HO_x production is balanced by a loss of one molecule of water vapor per H+OH pair. A summary of the reaction chains is provided, e.g., in Sinnhuber et al. (2012).

Changes in ozone. Bates & Nicolet (1950), for the first time, formulated that HOx catalytic cycles could constitute a key ozone loss mechanism. Similar mechanisms of catalytic ozone loss have been discussed for the terrestrial atmosphere and have been postulated for NOx (e.g., Crutzen 1970).

3. The Modified INCREASE Model Suite

An interpretation of upcoming atmospheric exoplanetary observations will need dedicated model studies taking into account processes such as the transport of stellar energetic particles (StEPs) and galactic cosmic rays (GCRs) through stellar astrospheres, planetary magnetic fields, and exoplanetary atmospheres, atmospheric escape, outgassing, climate, and (photo/ion) chemistry.

As a first step, Herbst et al. (2019, 2022a) built up the model suite INCREASE, a simulation chain that couples the state-of-the-art magnetospheric and atmospheric propagation and interaction models PLANETOCOSMICS (Desorgher et al. 2006) and AtRIS (Banjac et al. 2019) with the atmospheric chemistry and climate model 1D-TERRA (e.g., Scheucher et al. 2020b;
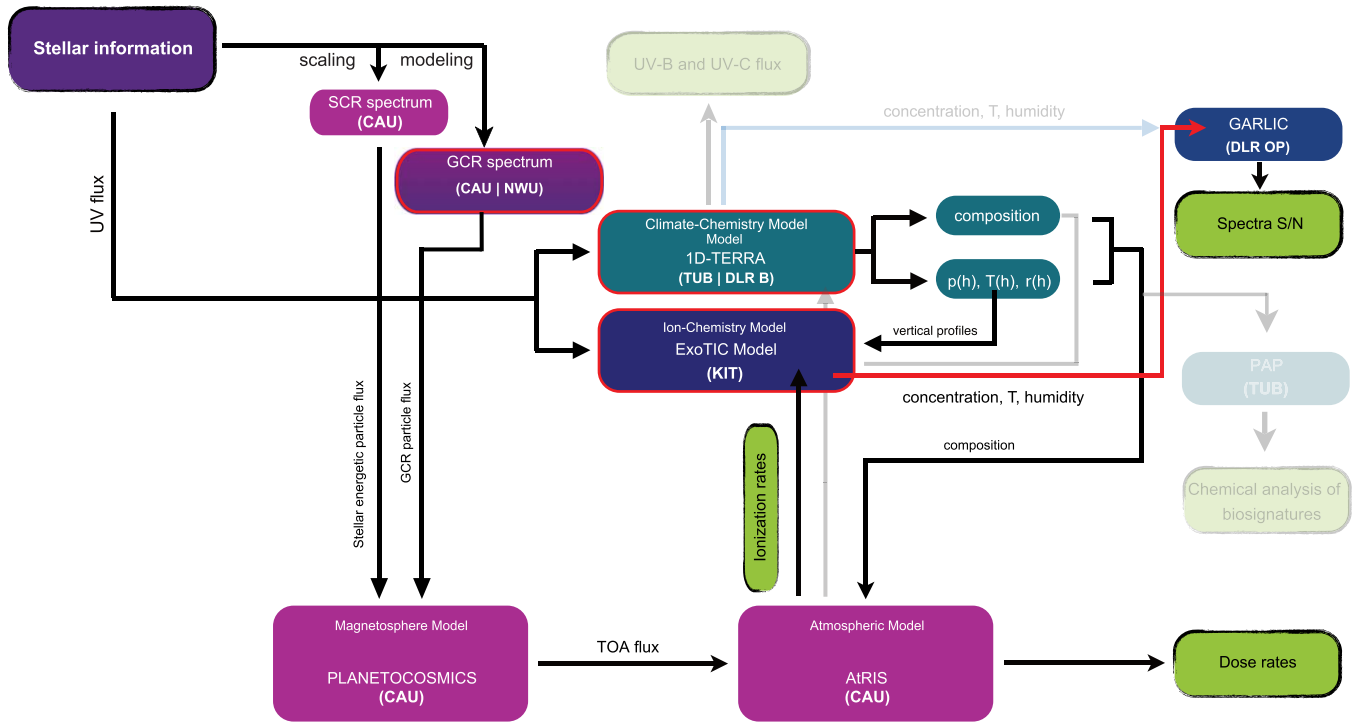
Figure 2. Interplay and output of the modified INCREASE model suite to study the impact of CRs on the atmospheric ion chemistry and induced changes to the spectral transmission features. Purple boxes highlight components derived and utilized at the University of Kiel (CAU). In contrast, dark blue boxes represent the models utilized by DLR Berlin and the Technical University Berlin (DLR/TUB). The light blue box represents the ExoTIC model maintained at the Karlsruher Institute of Technology (KIT), and the blue box highlights the GARLIC model maintained at DLR Oberpfaffenhofen. Green boxes show the output provided by the modified model suite. Unused branches and models of the full model suite (Herbst et al. 2019) are shown transparently; blocks with red outlines indicate updated models/codes; red arrows indicate newly added modeling steps.

Wunderlich et al. 2020) and the ion chemistry model ExoTIC (based on UBIC; see, e.g., Sinnhuber et al. 2012).

This study focuses on the impact of cosmic rays (CRs) on atmospheric ionization, ionization-induced changes in ion chemistry, and spectral transmission features. As shown in Figure 2, we slightly modified our model suite. We note that the parts of the full model suite described in Herbst et al. (2019) not used in this study are displayed transparently. Updated codes and models are highlighted by red outlining, while red arrows indicate newly added modeling steps. A brief description of the codes maintained at our institutes and the model coupling within the INCREASE model suite is given in what follows.

3.1. AtRIS

The Atmospheric Radiation Interaction Simulator (AtRIS; Banjac et al. 2019) is a GEANT4-based (Agostinelli et al. 2003) code to model the particle transport and interaction within exoplanetary atmospheres. We use AtRIS to model the cosmic ray induced atmospheric ionization rates and radiation dose profiles of diverse exoplanetary atmospheres.

3.2. PLANETOCOSMICS

AtRIS does not incorporate (exo)planetary magnetic fields. The location and altitude-dependent cutoff rigidity values—measures of the energy a particle must have to reach a specific location within the (exo)planetary atmosphere—are therefore simulated using PLANETOCOSMICS (Desorgher et al. 2006).

The particle fluxes atop the exoplanetary atmosphere are estimated depending on the computed values.

3.3. 1D-TERRA

The 1D-TUB model used in Herbst et al. (2019) has been considerably modified to the 1D Terrestrial Climate-Chemistry (1D-TERRA) column model (Scheucher et al. 2020b; Wunderlich et al. 2020). The radiative scheme was extensively revised to be valid for a wide range of exoplanetary atmospheres up to 1000 K and 1000 bar (e.g., Scheucher et al. 2020a). In the visible and infrared, up to 20 absorbers can be chosen, and overall, up to 81 UV/visible cross sections can be added. Rayleigh scattering and various continua can be added flexibly.

Wunderlich et al. (2020) further updated the flexible chemical network, which currently consists of 1127 reactions for 115 species. The scheme can consider wet and dry deposition and biomass, as well as volcanic and lightning emissions, and it features an adaptive eddy-diffusion coefficient profile based on atmospheric conditions.

3.4. ExoTIC

Because an ion chemistry network is not explicitly included in 1D-TERRA to study the effects of cosmic rays on atmospheric ion chemistry, we further coupled our models to ExoTIC, an adapted version of the University of Bremen Ion Chemistry column model (UBIC; Winkler et al. 2009; Sinnhuber et al. 2012; Nieder et al. 2014). ExoTIC is a 1D stacked box model of the neutral and ion atmospheric

composition. As of today, ExoTIC considers 60 neutral and 103 charged species (54 positive and 49 negative—including electrons), which interact due to neutral, neutral–ion, ion–ion gas-phase reactions, photolysis, and photoelectron attachment and detachment reactions (see, e.g., Sinnhuber et al. 2012). So far, ExoTIC has been extended to model (rocky) exoplanets with N_2–O_2 and CO_2-dominated atmospheres. Time-dependent photochemistry is driven by time-variable stellar flux based on the stellar spectrum and the planet's orbital motion and rotation. Particle impact ionization is considered a starting point for ion chemistry by dissociation, dissociative ionization, and ionization of N_2, O_2, and CO_2 as a function of time-dependent atmospheric ionization. Because the ions are much shorter-lived than the neutral species, the ion composition is calculated every six minutes as photochemical equilibrium, and formation/loss rates of the neutral species due to the ion composition are calculated and transferred to the neutral chemistry scheme. Since Herbst et al. (2019), the particle impact ionization, dissociative ionization, and ionization of CO_2,

$$CO_2 + e^* \longrightarrow CO_2^+ + e^- \tag{8}$$

$$CO_2 + e^* \longrightarrow CO^+ + O + e^- \tag{9}$$

$$CO_2 + e^* \longrightarrow CO + O, \tag{10}$$
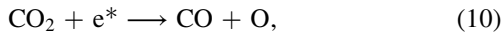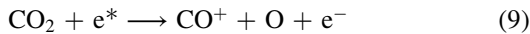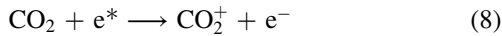
have been added to enable model experiments in CO_2-rich atmospheres.

3.5. GARLIC

The Generic Atmospheric Radiation Line-by-line Infrared Code (GARLIC; e.g., Schreier et al. 2014, 2018a, 2018b) is used for spectral analysis utilizing the atmospheric profiles (in particular, p, T, and the composition) derived within our model suite.

3.6. Model Coupling

This study focuses on the impact of cosmic rays on atmospheric ionization and ion chemistry. Therefore, we slightly modified the INCREASE model suite discussed in Herbst et al. (2019). As shown in Figure 2, to derive the results presented in Section 5, the following steps are performed: (1) measured stellar UV fluxes are used as input for 1D-TERRA and ExoTIC; (2) the incoming cosmic ray fluxes at the location of TRAPPIST-1e are derived either by analytic or numerical approaches (see Sections 2.1 and 2.2); (3) 1D-TERRA provides vertical profiles of temperature, pressure, and trace gases to ExoTIC and AtRIS; (4) to account for a potential planetary magnetic field, PLANETOCOSMICS is utilized to provide top-of-the-atmosphere (TOA) particle fluxes as input for the computations performed with AtRIS; (4) utilizing AtRIS, the GCR- and StEP-induced altitude-dependent radiation exposure and atmospheric ionization down to the exoplanetary surface are modeled; the latter is further used as input by ExoTIC; (5) with ExoTIC, the impact of changing atmospheric ionization for the different atmospheric compositions and parameterization of the neutral atmosphere is determined; (6) the changes in neutral–ion chemistry are computed with ExoTIC; (7) the resulting global atmospheric composition and temperature vertical profiles are utilized to compute atmospheric transit (primary) spectra with GARLIC.

4. Simulation Setup

4.1. Stellar Parameters and TRAPPIST-1 Spectra

In this study, we assumed a stellar effective temperature of $T_{eff} = 2516$ K (Van Grootel et al. 2018), a stellar radius of $R_\star = 0.124\ R_\odot$ (Kane 2018), a stellar mass of $M_\star = 0.089\ M_\odot$ (Van Grootel et al. 2018), and a distance of 12.43 pc (Kane 2018). Because the stellar spectral energy distribution in the (E)UV can strongly impact the photochemistry of terrestrial exoplanetary atmospheres (e.g., Grenfell et al. 2013; Tian et al. 2014), we use the semiempirical TRAPPIST-1 model spectrum by Wilson et al. (2021) based on observational data from XMM-Newton (X-ray regime) and from the Hubble Space Telescope (HST; in the 13–570 nm range), with a gap between 208 and 279 nm obtained through the Mega-MUSCLES Treasury survey (e.g., Froning et al. 2018; Wilson et al. 2019). Further, we use data from Wilson et al. (2021), who filled the higher-wavelength range based on a PHOENIX photospheric model (Baraffe et al. 2015; Allard 2016).

4.2. Scenarios for Planetary Atmospheres

TRAPPIST-1e has a radius of 0.92 $R_\oplus$ and a mass of 0.692 $M_\oplus$, and it orbits TRAPPIST-1 within 6.1 days at a distance of 0.02925 au.[9] Wunderlich et al. (2020) investigated multiple atmospheric scenarios for TRAPPIST-1 planets e and f. As a follow-up to their study, we utilize six of their discussed atmospheric compositions, adding the impact of cosmic rays to the picture to investigate their impact on the scenario-dependent atmospheric biosignatures. The following scenarios are assumed:

1. Dry-dead atmospheres, without an ocean and only taking into account volcanic outgassing, and thus assuming a relative humidity of 1% with 0.1 bar of CO_2 [1] (black solid lines) and 1 bar of CO_2 [2](black dashed lines).
2. Wet-dead atmospheres, with an ocean and only taking into account volcanic outgassing, and thus assuming a relative humidity of 80% without biosphere emissions and with 0.1 bar of CO_2 [3] (blue solid lines) and 1 bar of CO_2 [4] (blue dashed lines).
3. Wet-alive atmospheres, with an ocean and terrestrial biogenic and volcanic fluxes, similar to scenarios [3] and [4] with 0.1 bar of CO_2 [5] (green solid lines) and 1 bar of CO_2 [6] (green dashed lines), and high levels of oxygen from biogenic emissions.

Figure 3 shows the temperature profile of all investigated scenarios (colored solid lines), while Table 1 gives the surface pressure and scenario-dependent mass fractions of atmospheric CO_2, N_2, Ar, H_2O, and O_2 at the planetary surface that have been utilized as input for 1D-TERRA, AtRIS, and ExoTIC.

### 4.3. Modeling the Ion-chemistry Changes due to a Carrington-like Event

This study assumes TRAPPIST-1e to be a tidally locked planet and to have a stellar zenith angle fixed to 60° to mimic the global mean chemistry. Time-dependent experiments to model the impact of the Carrington-like event (see Section 2.2) for all six scenarios were carried out for 216 Earth hours, during which the stellar irradiance was considered constant. To

---

9 https://exoplanets.nasa.gov/exoplanet-catalog/3453/TRAPPIST-1-e/

Table 1
Scenario-dependent Mass Fractions of Atmospheric Constituents that Have Been Utilized as Input for AtRIS, 1D-TERRA, and ExoTIC

		$P_{surface}$ (hPa)	CO_2 (%)	N_2 (%)	Ar (%)	H_2O (%)	O_2 (%)	Others (%)
0.1 bar CO_2	dry-dead [1]	1031.62	13.3	84.0	1.3	3.47×10^{-4}	2.14×10^{-1}	1.19
	wet-dead [3]	1035.02	13.4	85.0	1.2	1.49×10^{-1}	7.01×10^{-3}	0.24
	wet-alive [5]	1036.45	12.8	51.7	1.2	1.95×10^{-1}	34.04	0.065
1 bar CO_2	dry-dead [2]	1879.76	61.1	34.4	1.0	2.24×10^{-3}	1.14	2.36
	wet-dead [4]	2043.32	63.0	32.0	1.0	0.3	4.27×10^{-3}	3.69
	wet-alive [6]	2079.23	61.2	1.13	1.0	3.82	32.77	0.08

Note. Scenario numbers are shown in square brackets.
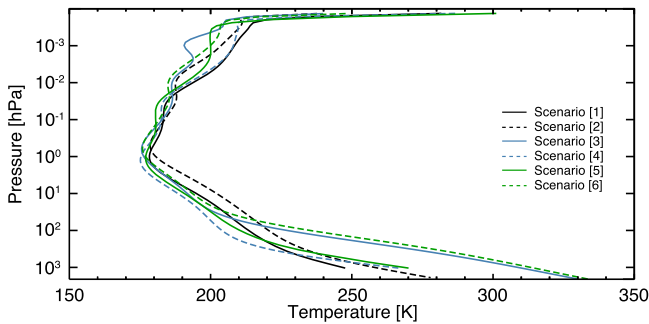
Figure 3. Temperature profile of the six scenarios discussed in Wunderlich et al. (2020; see Section 4.2, colored solid lines) in comparison to the terrestrial profile (dashed blue line).

Figure 4. Atmospheric ion pair production rates for scenarios [1]–[6] (colored lines) caused by GCRs (left side of the figure) and the Carrington-like event discussed in Vida et al. (2017; right side of the figure). In addition, the terrestrial production rate values during similar conditions are shown as blue dashed lines.
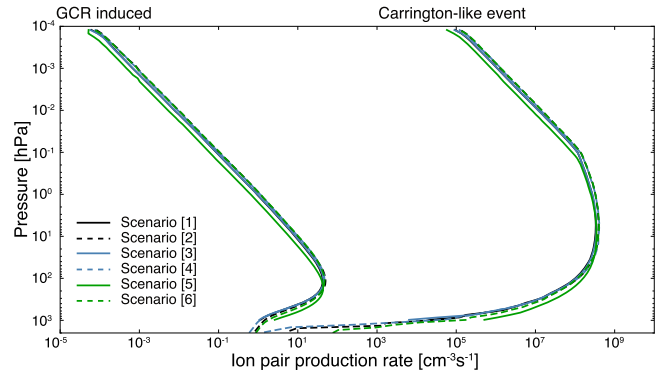
model the scenario-dependent ion-chemistry changes induced by the event, we implemented the corresponding ion pair production rate profiles provided by AtRIS (see results discussed in Section 5.1) for a time of six Earth hours after a spin-up period of 24 hr. As a first-order approximation, throughout these six hours, the stellar particle flux is assumed to be constant and zero otherwise, a simplification often used in solar–terrestrial studies to assess longer-lasting impacts of solar particle events (e.g., Jackman et al. 2000, 2005, 2011; Matthes et al. 2017). In addition, a model run without energetic particle impact and the particle event but identical in every other aspect was performed as a reference for each scenario.

5. Results

The following investigates the CR-induced changes in atmospheric ion pair production, ion chemistry, and composition.

5.1. The Cosmic-Ray-Induced Atmospheric Ion Pair Production Rate Changes

Figure 4 shows the modeled scenario-dependent CR-induced ion pair production rate values. As can be seen, the altitude of the GCR-induced production rate maximum varies from 200–100 hPa (12–15 km) (wet-alive 0.1 bar CO_2, green solid line) up to 100–50 hPa (15–22 km) (wet-dead 1 bar CO_2, dashed green line). Further, the production rate maximum values caused by the Carrington-like event are about 8 orders of magnitude higher than those during the quiet stellar conditions, and significant differences at the surface—depending on the atmospheric scenarios—occur. It shows that the higher the pressure (i.e., the CO_2 content), the lower the surface

production rates, due to CR shielding by CO_2. In particular, the Carrington-like event for the wet-dead 1 bar CO_2 scenario (in dashed blue) results in lower production rate values than the GCR-induced wet-alive 0.1 bar CO_2 scenario (in green).

5.2. The Cosmic-Ray-Induced Atmospheric Radiation Exposure

The resulting altitude-dependent absorbed dose rates of the six scenarios are shown in Figure 5. Here, profiles without energetic particle impact (left side of the figure) and caused by the Carrington-like event (right side) are displayed. As can be seen, all scenarios are similar within ±2% at altitudes above 10 hPa (40 km) (1 hPa (55 km)) during quiescent stellar conditions (during the Carrington-like event).

In the CO_2-rich scenarios [2, 4, 6], a Carrington-like event only leads to comparatively negligible radiation exposure increases at the planet's surface. However, in the CO_2-poor scenarios [1, 3, 5], in particular within the wet-alive atmosphere, a Carrington-like event would lead to more than 3–4 orders of magnitude increase at the planetary surface. As listed in Table 2, in the CO_2-poor wet-alive case, the Carrington-like event would lead to absorbed dose rates around 1.69 mGy hr^{-1}, which is more than 23,300 times higher than those during the actual Carrington event at the terrestrial surface. To put this into perspective, we note that chromosomal aberrations and mutations can already occur at dose rates between 1 and 20 mGy hr^{-1}, which corresponds to accumulated doses of 0.5–8 Gy (e.g., Rühm et al. 2018, and references therein). Thus, although a Carrington-like event in a CO_2-poor wet-alive atmosphere would lead to changes at the DNA level, it would not be lethal.
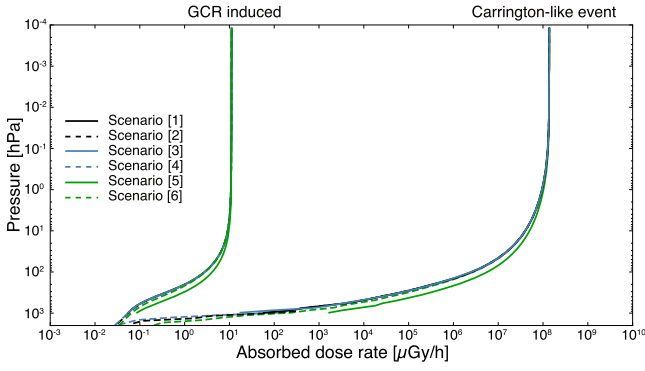
Figure 5. Averaged atmospheric absorbed dose rates for scenarios [1]–[6] (colored lines) caused by GCRs (left side of the figure) and the Carrington-like event discussed in Vida et al. (2017; right side of the figure). In addition, the terrestrial absorbed dose rates during similar conditions are shown as blue dashed lines.

Table 2
Absorbed Dose Rate Values

	Scenario	D_{GCR} (μGy hr^{-1})	D_{SEP} (μGy hr^{-1})
0.1 bar CO_2	[1]	5.54×10^{-2}	5.85×10^{1}
	[3]	5.51×10^{-2}	1.76×10^{1}
	[5]	8.68×10^{-2}	1.69×10^{3}
1 bar CO_2	[2]	3.24×10^{-2}	7.42×10^{-2}
	[4]	2.85×10^{-2}	3.54×10^{-2}
	[6]	3.45×10^{-2}	2.14×10^{-1}

Note. Absorbed rate values are at the surface of TRAPPIST-1e for the Earth-like atmosphere scenarios [1]–[6] during stellar quiet conditions (D_{GCR}) and the Carrington-like event (D_{SEP}) scaled after Vida et al. (2017)

5.3. Atmospheric Ion Chemistry and Composition Changes

The impact of the Carrington-like event on the atmospheric chemical composition of scenarios [1]–[6] is shown in the panels of Figure 6, displaying the difference between the mean volume mixing ratios [ppm/ppb] with and without ion chemistry during the event, for which an event period of 6 hr is assumed. This allows us to visualize the production and destruction of individual species due to the impact of atmospheric ionization and subsequent ion and neutral chemistry.

5.3.1. Water Loss and HOx Formation

As shown in Figure 6, results suggest the destruction of water vapor (H_2O; panel (a)) throughout the entire atmosphere, which can be explained by the uptake of water vapor in positive water cluster ions that ultimately leads to the formation of HOx during recombination of the water cluster ions (Sinnhuber et al. 2012). The loss of water vapor is mirrored by an increase of HOx of comparable size, as shown in panel (b). The relatively high water-loss values in the dry-dead scenarios [1, 2] result from greater amounts of water vapor in the middle atmospheres above 200 hPa (10 km).

5.3.2. Methane Change

At around 10–0.01 hPa (40–70 km), the HOx formed by the ion chemistry is mainly in the form of hydroxyl (OH; panel (c)). Hydroxyl acts as a sink for methane (CH_4; panel (d)) via
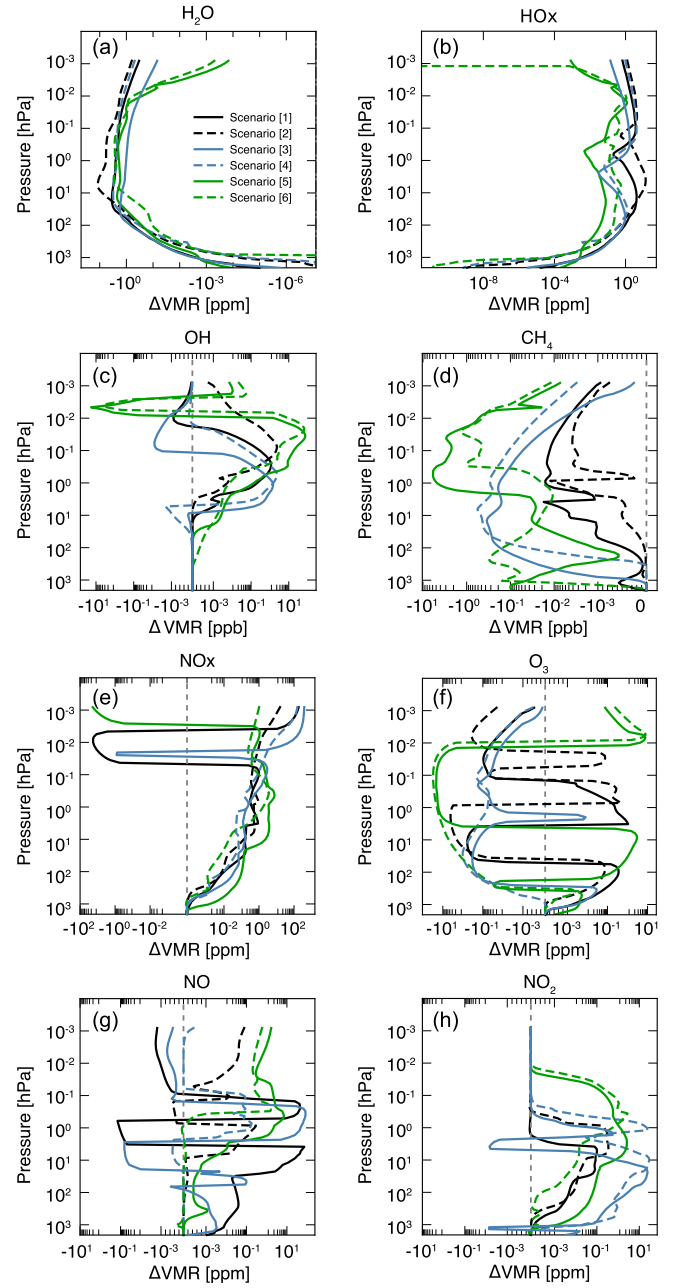
Figure 6. Absolute differences between model experiments with and without atmospheric ionization for the time of a six-hour Carrington-like stellar particle event modeled with ExoTIC.

the reaction $CH_4 + OH$, and a decrease of methane over nearly the whole model altitude is evident, maximizing in the altitudes where the OH increase is most prominent in the respective scenario. The largest increases in OH, and respective decreases in methane, are observed in the wet-alive scenarios [5, 6] between 0.1–0.01 hPa (50–70 km), due to more available O_2 and H_2O.

5.3.3. Ozone Change

Based on the strong increase in HOx from 0.01–10 ppm at 200–0.01 hPa (10–70 km) in all scenarios, as well as the increase of NOx of a few ppb to several ppm depending on scenario and altitude (see panels (e), (g), and (h) of Figure 6), a loss of ozone would be expected over a wide range of altitudes

for all scenarios. The change in ozone for all six scenarios is shown in panel (f). As can be seen, ozone loss is observed in all scenarios. However, the altitude range differs considerably between the various scenarios, with different regions of ozone formation in some altitudes and scenarios. For example, for the CO_2-rich wet-dead scenario [4], ozone loss extends nearly over the whole altitude range, from about 200 hPa (10 km) to the top of the model boundary above 0.01 hPa (80 km). In contrast, for the CO_2-poor wet-alive scenario [5], ozone loss is also observed in 10–0.01 hPa (40–70 km), while above and below this altitude range, ozone formation is observed. The CO_2-rich wet-alive scenario [6] shows a similar behavior, with a larger area of ozone loss than the CO_2-poor scenario between 200–0.01 hPa (15–70 km) but similar regions of ozone formation above and below. In the dry-dead scenarios [1, 2] and in the CO_2-poor wet-dead [3] scenario, ozone loss and ozone formation regions alternate between 200 hPa (10 km) and 0.01 hPa (70 km), with ozone loss dominating at the top. Ozone formation at altitudes above 0.01 hPa (70 km) is likely due to dissociation of O_2 by charged particle impact ionization with subsequent ozone formation via $O + O_2$ in the oxygen-rich atmospheres of the wet-alive scenarios [5, 6] at altitudes where water vapor is not abundant and HOx formation is therefore small (see Figure 6(b)). Another mechanism of ozone formation that could be initiated by atmospheric particle impact ionization is the so-called smog mechanism, where the photodissociation of NO_2 in the visible spectral range provides atomic oxygen (O) for ozone formation. Similar reaction chains lead to ozone formation, especially in the polluted summer troposphere of Earth, but not in the terrestrial stratosphere and mesosphere, where the availability of atomic oxygen from photolysis of O_2 in the far-UV spectral range enables catalytic ozone loss involving NOx (e.g., Lary 1997). The M dwarf TRAPPIST-1 has a much redder spectrum than the Sun, with significantly lower radiative fluxes in the UV spectral range. Therefore, photodissociation of O_2 is negligible, and the formation of NOx by particle impact ionization leads to ozone formation via the smog mechanism rather than catalytic ozone loss as in the terrestrial stratosphere. Catalytic ozone loss via HOx does not depend on the availability of atomic oxygen (Lary 1997), and it can also occur in our scenarios. Therefore, distinction between ozone loss and ozone formation depends critically on the availability of NOx, HOx, and—only in the upper part of the atmosphere—O_2, leading to the layering of ozone formation and loss calculated, e.g., in the dry-dead scenarios [1, 2], and to the distinctive difference between the CO_2-rich [6] and CO_2-poor [5] wet-alive scenarios, which differ in the amount of HOx production above 100 hPa (15 km).

The upper panel of Figure 7 shows the total ozone column density, reflecting the consequences of ozone loss versus ozone formation: At the start of the event, ozone loss becomes apparent in most scenarios. However, the CO_2-poor dry-dead [1] and wet-alive [5] scenarios differ from the other scenarios and show an increase in total column ozone. These scenarios show particularly strong ozone increases around 100–10 hPa (15–40 km) (see also Figure 6(f)) at the lower edge of the ozone layers in these particular atmospheres where relative changes in ozone have the largest impact on the total column amount. This is also indicated in the CO_2-rich dry-dead scenario [2]. However, ozone formation around 90 hPa (20 km) is smaller
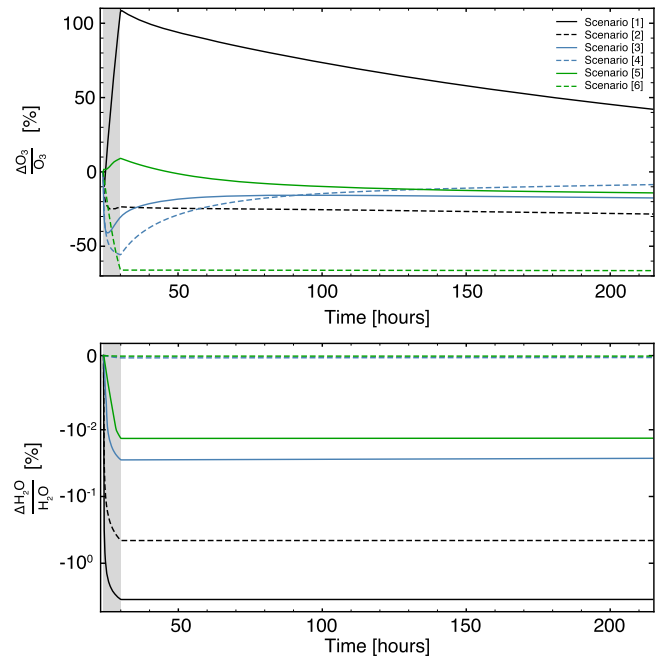
Figure 7. Time series of the deviation in the O_3 column density (upper panel) and the H_2O column density (lower panel) for the six scenarios during (gray bar) and after the particle event.

—and therefore does not lead to production in the total ozone column.

The evolution of ozone after the particle event is determined by a sensitive balance of production and loss mechanisms involving the amount of O, HOx, and NOx available at the end of the event, as well as the solar irradiance spectrum. Relevant mechanisms include ozone loss by the short-lived HOx as well as ozone formation by the much longer-lived NOx in the lower part of the atmosphere, by atomic oxygen in the upper part of the atmosphere, and by UV photolysis of O_2 and CO_2 in the upper part of the atmosphere. Ozone loss and formation by HOx and NOx can further be modulated by the formation of HNO_3 via the reaction $OH+NO_2$, which reduces both HOx and NOx. Consequently, the evolution of ozone after the event is very different in the different scenarios. After the event, ozone columns recover to a value similar to the starting point over the course of a few days in the wet-dead scenarios [3, 4] and the CO_2 poor wet-alive scenarios [5]. In scenario [1], total ozone recovers from strongly enhanced values much more slowly and is still greatly enhanced at the end of the model period, while in the CO_2-rich dry-dead [2] and wet-alive [6] scenarios, ozone stays greatly depleted, without any recovery throughout the model period. In these two scenarios, the formation of NOx in the lower part of the atmosphere where the NOx-driven ozone formation dominates is comparatively low due to the lower amount of N_2 available in the CO_2 rich scenarios, while the amount of HOx produced is high. Additionally, the lower panel of Figure 7 shows the relative changes of the H_2O column density. As in Figure 6(a), water loss of up to 2% during the event can be observed, especially for the dry and dead scenarios [1, 2]. However, the column density calculation is dominated by the lower parts of the atmosphere, so the percentage change of the total water column is small (see Table 1). This is especially true for the wet scenarios [3–6]. The water content does not recover within the model experiment period, as HOx preferentially forms H_2, not water vapor.
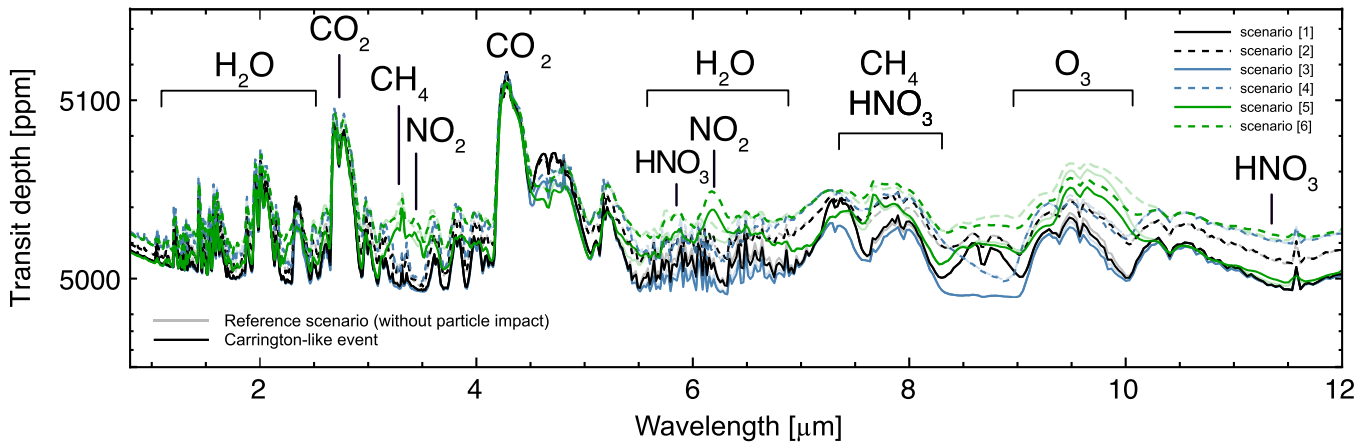
Figure 8. Modeled scenario-dependent transit depths of TRAPPIST-1e in parts per million (ppm) over wavelength λ ($R = 300$), showing the spectra without energetic particle impact (solid lines) and during the Carrington-like event (dashed lines).

Thus, the impact of a Carrington-like event and the corresponding particle impact ionization on the transmission spectra can likely be long-lasting in some scenarios—and might be considered in particular in the surroundings of a very active star with frequent flares. The varying response of the total amount of ozone during and after the particle event will have implications for the transmission spectra and limit the usability of ozone as a biosignature in planets orbiting active cool stars if the atmospheric composition is not characterized very well.

5.4. Consequences for the Transmission Spectra

Figure 8 shows the transmission spectra of the six scenarios generated with GARLIC (Schreier et al. 2014, 2018a, 2018b), neglecting the impact of energetic particles (reference case, weak lines) and the Carrington-like event (strong line). Thereby, the time mean over the 6 hr event period was used to calculate the mean atmospheric state. GARLIC used a resolving power of $R = 300$ to generate the transmission spectra (see Wunderlich et al. 2020). As can be seen, the Carrington-like event—highlighting the impact of the enhanced atmospheric ionization on the transmission spectra—leads to significant changes in the scenario-dependent transmission spectra.

For better visibility, Figure 9 shows the spectra during the Carrington-like event in the first (0.8–4.0 μm) and third panels (4.0–12.0 μm). In contrast, the differences between the respective spectra and the reference case neglecting the impact of energetic particles are displayed in the second and fourth panels, respectively.

To help identity which trace gases contribute to the spectral signatures identifiable in Figure 9, the Jacobian, i.e., the partial derivatives of the effective height w.r.t. to the scale factor α of the molecular density, of the effective height spectra regarding the trace gases are shown in Figure 10 (colored lines, here for $\alpha = 1$; see Schreier et al. 2015, Section 3.3 for further information). In the spectral range 0.7–4 μm, overlapping signatures of CO_2 (1–1.1, 1.2–1.4, 1.4–1.7, 1.8–2.3, 2.4–3.2, 3.5–4 μm), CH_4 (1.6–1.83, 2.1–2.7, 3.0–4.0 μm) and H_2O (1.1–1.25, 1.25–1.6, 1.7–2.0, 2.1–2.7, 2.8–3.4 μm) dominate, with smaller contributions of O_3 (3–3.8 μm) and NO_2 (3.4–3.5 μm) masked by the larger signals.

In the range 4–12 μm, spectral signatures of CO_2 (4–5.5 μm, 7–8.3 μm, 8.9–12 μm), CH_4 (5.8–9.2 μm), H_2O (4.9–7.7 μm), and O_3 (8.1–10.4 μm) dominate, with smaller contributions from HNO_3 (4.7–6, 7.3–7.8, 8.1–8.5, 8.8–12 μm), NO_2 (6–6.4 μm), and NO (5–5.7 μm). Thus, for example, the strong water signal at 2.1–2.7 μm overlaps with the CO_2 band at 2.4–3.2 μm, which is weaker in the maximum of the H_2O band around 2.4–2.7 μm, while the broad water vapor band at 4.9–7.7 μm overlaps with narrower signals of NO (5.0–5.7 μm), HNO_3 (4.7–6.0 μm), and NO_2 (6.0–6.4 μm).

However, due to the impact of the Carrington-like event, the reduction of H_2O reduces the atmospheric transit depth in all water bands, with the most significant reduction of up to 15% between 5.5 and 7.0 μm (see the fourth panel of Figure 9). In particular, the CO_2-poor runs [1, 3, 5] show a larger difference in the spectral features of H_2O than discussed in Wunderlich et al. (2020). While Wunderlich et al. (2020) found a difference between scenarios [1] and [5] on the order of 12 ppm, this study shows a difference of 42 ppm, which can be directly attributed to the additional influence of ion chemistry in the upper atmosphere induced by the stellar event. Of further importance within the 5.0–7.0 μm H_2O band are the two significant peaks around 5.2–5.6 μm (NO) and 6.0–6.5 μm (NO_2) showing deviations from the reference scenario of up to 40% (fourth panel of Figure 9). While the increase in NO is mainly observed in the CO_2-poor wet-alive scenario [5], the increase in NO_2 is present in all scenarios. The latter is consistent with the formation of NO_2 up to 0.02 hPa (65 km), but it is most vital in the two wet-alive scenarios [5, 6]. These two scenarios further show an increase in the HNO_3 signal at 5.5–6.0 μm. Here, the combined impact of the increase of the NO, HNO_3, and NO_2 signals masks the decrease of the water band signal in both scenarios.
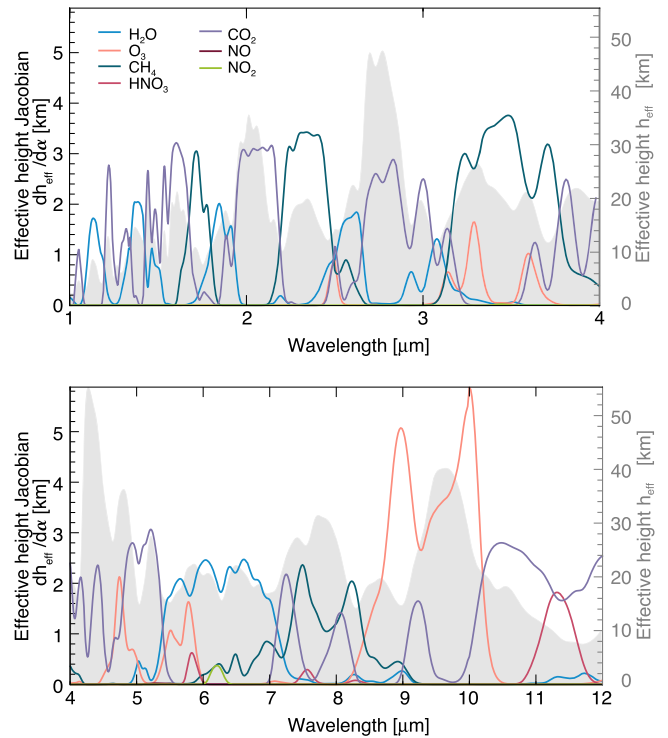
A decrease of up to 10% is shown in the methane band at 3.0–3.7 μm, consistent with the decrease of methane due to the increased OH. However, loss of ozone could contribute to this as well, in particular the narrow features at ~3.3 and 3.6–3.7 μm. A small positive feature in 3.3–3.5 μm overlapping with the methane band can be attributed to another smaller NO_2 band, emphasizing the substantial increase of NO_2, in particular in the CO_2-rich dry-dead scenario [2] and in the two wet-alive scenarios [5, 6]. Conversely, the methane band at 7.0–8.5 μm appears to increase. This is due to the increase of the HNO_3 band (at 7.3–7.8 μm), which nearly perfectly overlaps with the maximum of the CH_4 band, shadowing the methane decrease in the spectrum. The increase of HNO_3 is also highlighted by the increase of the HNO_3 band at 11.0–12.0 μm, which reaches up to 25% for the CO_2-poor wet-alive scenario [5]. The O_3 band at 9.0–10.0 μm is reduced by
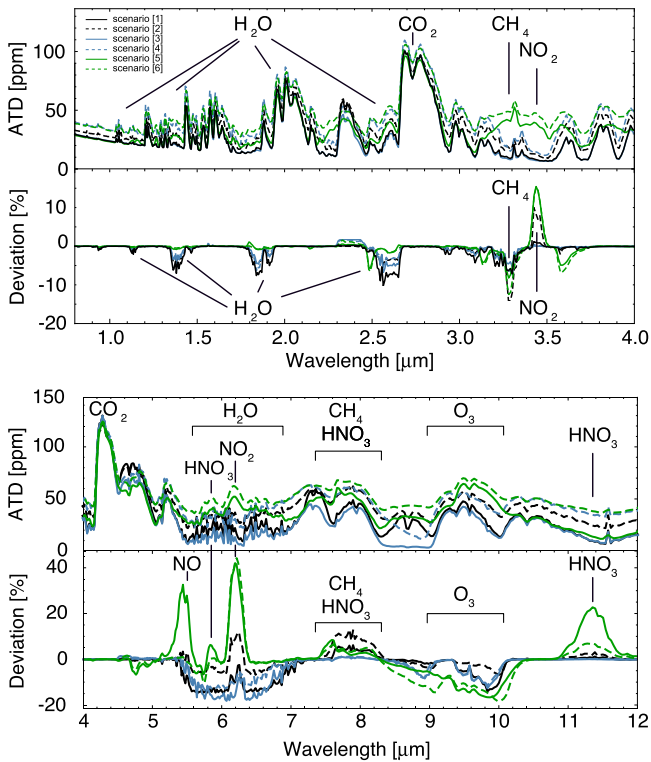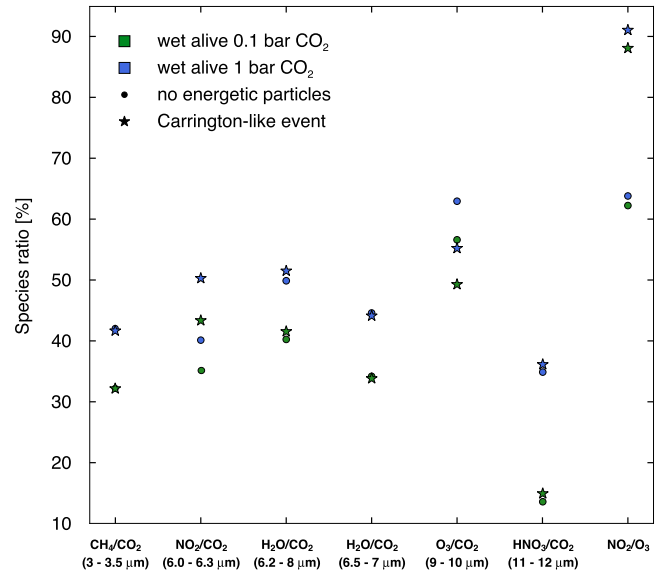
Figure 9. Resulting transmission spectra of the six scenarios discussed in Section 4.2, based on the mean atmospheric composition during the 6 hr Carrington-like event (Panels 1 and 3 in Atmospheric Transit Depth (ATD)). The second and fourth panels show the deviation (with ions - without ions) in each transmission spectra, compared to a corresponding reference run without ion chemistry.

Figure 10. Jacobian of the effective height spectra of the trace gases shown in Figure 13 ($R = 100$). Gray areas: Effective height—the altitude where the atmosphere becomes optically dense ($\tau > 1$)—indicating that, in the 4–12 μm range, the spectral signatures all derive from the middle atmosphere above 9 km. Colored lines: the derivatives of the effective heights to the most important species, a measure of the contribution of the trace gases to the spectral signal. Shown as an example is the CO_2-poor wet and alive scenario ([5]).

10 to 20% in all scenarios, most strongly for the wet-alive scenarios [5, 6] with the highest oxygen amounts—and therefore O_3 values—at the beginning of the model period. This is counterintuitive because we calculate strong increases in ozone at certain altitudes—and even in total ozone in some scenarios. This is because the ozone signals derive from the middle atmosphere above 20 km altitude, as indicated by the effective height shown in Figure 10. In contrast, the total ozone column is more sensitive to the atmospheric parts below 100 hPa (20 km).

For a clearer characterization of potentially measurable signatures, Figure 11 shows the ratios of individual spectral bands to the CO_2 band between 4.2 and 4.5 μm. CO_2 remains almost constant in all investigated scenarios and is therefore well suited as a reference band. When comparing with the CO_2 band, the most significant differences between model runs with and without the particle event are shown for the NO_2 to CO_2 and O_3 to CO_2 ratios, while for CH_4 and HNO_3 there are no significant differences in this wavelength range. The selection of band boundaries also plays a role; an example is the water band, where for band boundaries from 6.2 to 8.0 μm, including the whole band, the ratio increases for the model results with particle event, while for the more narrow selection of 6.5–7.0 μm, the ratio decreases, which is caused by a contamination with NO_2 at 6.2–6.3 μm in the first case. In Earth-like atmospheres, with a high proportion of N_2 and O_2, the ratio of NO_2/O_3 shows a large difference between cases with and without particle events—and could therefore be used to characterize observations in the vicinity of a flaring star. Detecting such small signals, however, would be very challenging for the JWST.


Figure 11. Ratio of individual spectral bands with respect to the CO_2 feature from 4.2 to 4.5 μm for the two wet-alive scenarios [5, 6] with the greatest differences in potential biosignatures compared between the Carrington-like event versus no energetic particles.

5.5. Comparison to Previous Model Efforts

A recent study by Mikal-Evans (2022) discussed the possibility of observing the potential biosignature redox pair CH_4–CO_2 in the atmosphere of TRAPPIST-1e with the help of JWST. Utilizing the publicly available petitRADTRANS code (Mollière et al. 2019),
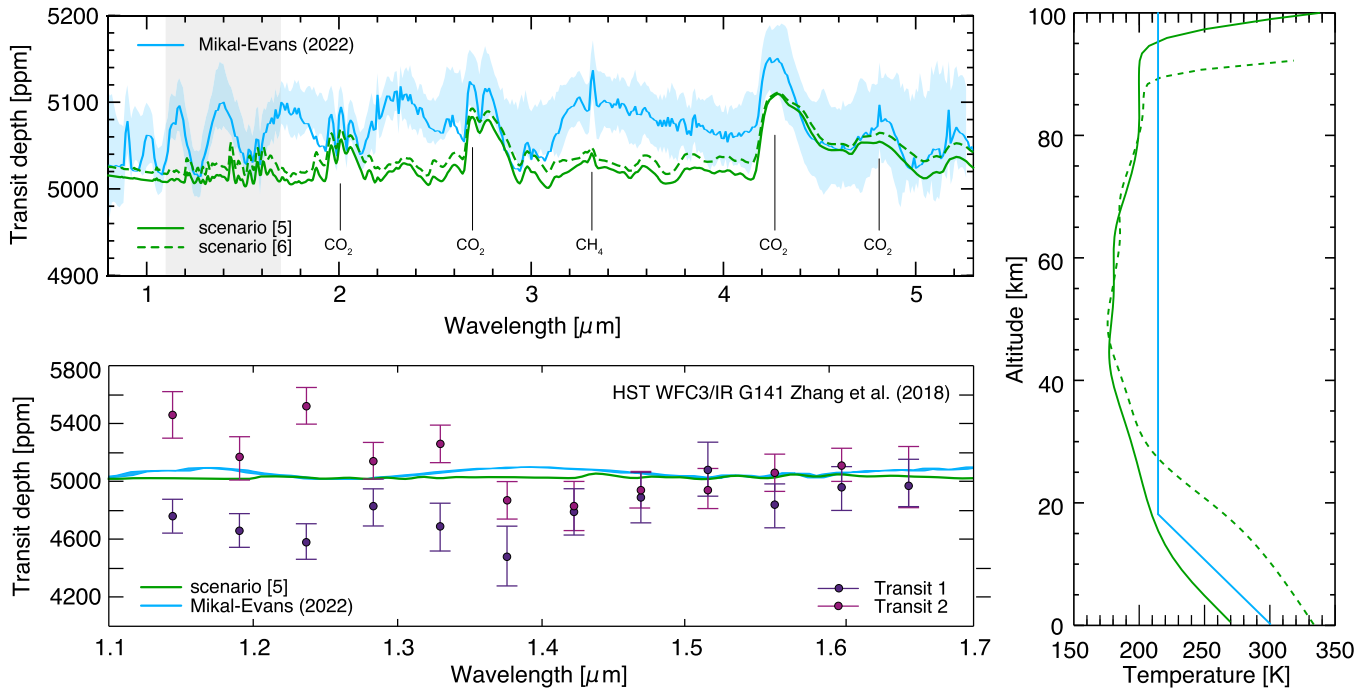
Figure 12. Upper left panel: Comparison of our work to the model results of Mikal-Evans (2022), who assumed a cloudless Archean Earth. Gray shading indicated the wavelength range of the bottom left panel. Lower left panel: The transmission spectra of TRAPPIST-1e observed with HST/WFC3 during two different transits (see Zhang et al. 2018). The green lines show our wet-alive model results during the Carrington-like event (solid lines—scenario [5], dashed lines—scenario [6]), while the blue lines correspond to the Archean Earth scenario of Mikal-Evans (2022). Right panel: Comparison of the corresponding assumed atmospheric temperature profiles.

transmission spectra for an Archean-like TRAPPIST-1e were derived. Mikal-Evans (2022) concluded that, under the premise of reliable instrument noise and disregarding the impact of stellar variability, robust (5σ) detections of both CH_4 and CO_2 for 5–10 transit observations are feasible. The upper left panel of Figure 12 compares the cloud-free model results by Mikal-Evans (2022; in blue) and our wet and alive scenarios neglecting the impact of energetic particles. In contrast, the right panel compares the scenario-dependent temperature profiles. As expected, the results vary due to the different assumptions (i.e., Archean Earth versus modern Earth scenarios). However, the modeled CO_2 features agree and align well with the derived JWST/NIRSpec transmission spectra simulations (blue shaded area), assuming ten transits.

5.6. Comparison to HST Observations

In a study by Zhang et al. (2018), the near-infrared transmission spectra (1.1 and 1.7 μm) of TRAPPIST-1e observed with the Hubble Space Telescope (HST) Wide Field Camera 3 (WFC3) during two transits—separated by 12 days —were discussed. As shown in the lower left panel of Figure 12, above 1.4 μm, no spectral differences between the two transits can be seen. In the wavelength range <1.35 μm, however, differences of up to 650 ppm are present. One possible explanation was a "temporal variability of stellar contamination" (Zhang et al. 2018). Assuming the studied atmospheres to be valid representations, we find a good agreement between the observations and our model results— shown here as an example is the transition spectrum of the wet-alive 0.1 bar CO_2 scenario (solid green line)—at wavelengths above 1.35 μm. The same applies to the Archean Earth scenario discussed in Mikal-Evans (2022; blue line). However, none of our scenarios show a cosmic ray induced variation below 1.35 μm, thus ruling out contamination of the transmission spectrum due to a Carrington-like event, as discussed in this

study. However, more advanced studies, e.g., including variable exoplanetary magnetic fields and their response to potential coronal mass ejections passing the planet, will be required in the future.

6. Summary and Conclusions

With the help of our model suite INCREASE (Herbst et al. 2019, 2022a), we investigated the impact of cosmic rays (i.e., GCRs and StEPS) on atmospheric ionization, radiation exposure, and ion chemistry—and with that, the spectral transmission features of TRAPPIST-1e. Because its atmospheric composition is yet to be confirmed, we used six scenarios varying between dry-dead, wet-dead, and wet-alive conditions, assuming either CO_2-poor (0.1 bar) or CO_2-rich (1 bar) scenarios (see Wunderlich et al. 2020).

Due to the lack of in situ particle measurements, we, for the first time, utilize a 1D SDE code to derive GCR proton and helium fluxes at the location of TRAPPIST-1e, showing the particle spectra to be comparable to spectra measured at Earth during very low solar activity phases. Therefore, GCRs form a nonnegligible production background concerning atmospheric ionization and radiation exposure, and with that, cannot be neglected in the context of (ion) chemistry, climate, and habitability. Furthermore, to study the impact of stellar energetic particles, the famous Carrington event has been scaled to the orbit of TRAPPIST-1e (see discussion in Vida et al. 2017) and extended to energies up to 40 GeV. Because of the resulting high particle fluxes, we showed that the event-induced scenario-dependent atmospheric ionization and radiation exposure can be up to 7 orders of magnitude higher than the GCR-induced values at the ionization maximum (see Figures 4 and 5).

As shown in Figure 6, an enhancement of the ionization rates drastically impacts atmospheric ion chemistry. We found that,

for all six scenarios, the NOx production is comparable to terrestrial values induced by strong particle events. We further found CRs to strongly impact ozone in all investigated scenarios. For instance, for the CO_2-rich wet-dead scenario [4], ozone loss can be observed from 200 hPa (10 km) onward, while in the CO_2-poor wet-alive scenario [5], ozone production is observed at altitudes below 10 hPa (40 km). We found that the CO_2-poor dry-dead scenario [1] and the CO_2-poor wet-alive scenario [5], in particular at the beginning of the event, differ from the other scenarios by showing an increase in the total ozone column density (i.e., around 100–10 hPa (15-40 km)). Further, we found that—in contrast to the other scenarios—the total ozone column density of scenarios [1] and [6] does not recover to background values within a few days after a Carrington-like event, which could strongly impact the transmission spectra of Earth-like exoplanets around active M dwarfs with frequent flaring (see also Herbst et al. 2019; Scheucher et al. 2020a). We also showed that a Carrington-like event would lead to the destruction of water vapor and the production of HOx throughout the entire atmosphere and that hydroxyl acts as a methane sink in the wet-dead scenarios [3, 4] (most prominent features are found within 90–10 hPa (20–50 km)) and the wet-alive scenarios [5, 6] (most prominently around 10–0.05 hPa (50–70 km)).

This work further illustrates the challenges of forthcoming transmission spectral analysis and the caution with which these spectra must be interpreted, especially in the case of Earth-like exoplanets orbiting active stars. In the scenario-dependent GARLIC-based synthetic planetary transmission spectra (Figures 8 and 9), we found the following key features:

(1) All scenarios show large event-induced amounts of NO_2 at 6.2 μm, most visible in scenarios [5, 6] with an increase of 40% compared to the reference case neglecting the impact of energetic particles.

(2) All scenarios show an event-induced reduction of the atmospheric transit depth in all water bands, most prominently seen for the H_2O band between 5.5 and 7.0 μm, with a decrease of up to 15% in all six scenarios.

(3) Because of the simulated Carrington-like event, a decrease of up to 10% in the methane band at 3.0–3.5 μm is present in all scenarios. In the case of scenarios [2, 5, 6], however, this feature is masked by the increase of NO_2 at 3.3–3.5 μm. At first sight, the CH_4 band at 7.0 μm appears to increase—this increase, however, is actually caused by a strong HNO_3 band induced by the stellar energetic particles, which nearly perfectly overlaps with the spectral range of the CH_4 band, shadowing the methane decrease in the spectrum.

(4) Ozone features are rather weak for scenarios around mid-to-late M dwarfs (e.g., Scheucher et al. 2020a). This is mainly due to changes in the incoming stellar radiation leading to a reduction in ozone abundance and spectral absorption (e.g., Segura et al. 2005; Grenfell et al. 2012). All scenarios show a depletion of ozone at 9.0–10.0 μm on the order of 10% to 20%. The amount of ozone loss is due to a sensitive balance between the formation of HOx, NOx, and atomic oxygen during the event, and therefore it depends critically on the availability of atmospheric water vapor, N_2, and oxygen.

(5) The buildup of the HNO_3 spectral feature at 11.0–12.0 μm, which previously has been reported to be a potential proxy of stellar particle contamination in all
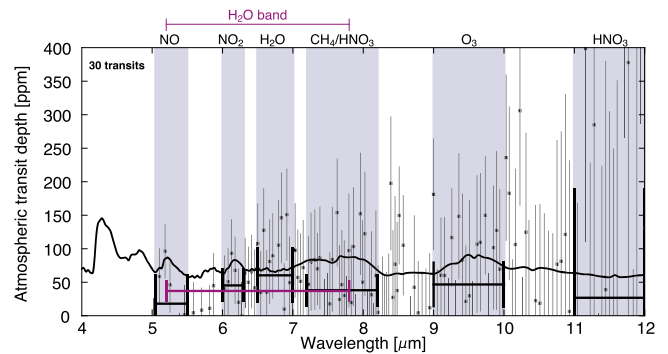
Figure 13. Modeled JWST Mid-Infrared Instrument (MIRI) Low Resolution Spectroscopy (LRS) 30 transit transmission spectrum (dots) based on the CO_2-poor wet and alive scenario (solid black line).

N$_2$-O$_2$-dominated atmospheres (e.g., Tabataba-Vakili et al. 2016; Scheucher et al. 2018; Herbst et al. 2019; Scheucher et al. 2020a) is absent in the wet-dead scenarios [3, 4].

(6) In the case of a CO_2-poor, wet-alive, Earth-like atmosphere, a strong event-induced NO feature at 5.5 μm is present. A similar feature can be found in the study by Scheucher et al. (2020a) investigating the impact of CRs on the Earth-like atmosphere of Proxima Centauri b.

As discussed in Wunderlich et al. (2020), the described scenarios may be differentiated under cloud-free circumstances by combining 30 transit observations with JWST NIRSpec. Using PandExo (Batalha et al. 2017), we simulated JWST MIRI LRS observations of TRAPPIST-1e based on our wet and alive 0.1 bar CO_2 scenario during 1–100 transits (see Figure 13 showing the results of the 30 transit run). In the case of the CO_2-poor, wet, and alive scenario, we find that to detect the O_3, NO_2, and H_2O features, 30 or more transits are necessary.

Unfortunately, even with 100 transits, the HNO_3 feature at 11–12 μm, which is a direct measure of the impact of cosmic rays on Earth-like atmospheres in our dry-dead and wet-alive scenarios [1, 2, 5, 6], is not detectable with JWST MIRI, due to the large signal-to-noise ratio in thermal IR. However, detecting such a feature is mandatory in order to distinguish whether the observed biosignature signals have been contaminated by the impact of stellar energetic particles. Therefore, future missions like the Origins Space Telescope (OST; see https://origins.ipac.caltech.edu/download/MediaFile/171/original Mission Study Concept Report), ELT (e.g., Neichel et al. 2018), and LIFE (e.g., Quanz et al. 2022) are essential.

ORCID iDs

Konstantin Herbst ● https://orcid.org/0000-0001-5622-4829
Andreas Bartenschlager ● https://orcid.org/0000-0002-8631-7572
John Lee Grenfell ● https://orcid.org/0000-0003-3646-5339
Nicolas Iro ● https://orcid.org/0000-0003-2329-418X
Miriam Sinnhuber ● https://orcid.org/0000-0002-3527-9051
Benjamin Taysum ● https://orcid.org/0000-0002-0856-4340
Fabian Wunderlich ● https://orcid.org/0000-0002-2238-5269
N. Eugene Engelbrecht ● https://orcid.org/0000-0003-3659-7956
Juandre Light ● https://orcid.org/0000-0002-9788-5540
Katlego D. Moloto ● https://orcid.org/0000-0002-4840-6355
Jan-Vincent Harre ● https://orcid.org/0000-0001-8935-2472
Heike Rauer ● https://orcid.org/0000-0002-6510-1828
Franz Schreier ● https://orcid.org/0000-0001-7196-6599

References

Agostinelli, S., Allison, J., Amako, K., et al. 2003, NIMPA, 506, 250
Allard, F. 2016, SF2A-2016: Proc. of the Annual meeting of the French Society of Astronomy and Astrophysics, ed. C. Reylé, L. Cambrèsy, M. Deleuil et al., 223
Alvarado-Gómez, J. D., Drake, J. J., Moschou, S. P., et al. 2019, ApJL, 884, L13
Banjac, S., Herbst, K., & Heber, B. 2019, JGRA, 124, 50
Baraffe, I., Homeier, D., Allard, F., & Chabrier, G. 2015, A&A, 577, A42
Barth, P., Helling, C., Stüeken, E. E., et al. 2021, MNRAS, 502, 6201
Batalha, N. E., Mandell, A., Pontoppidan, K., et al. 2017, PASP, 129, 064501
Bates, D. R., & Nicolet, M. 1950, JGR, 55, 301
Bourrier, V., Ehrenreich, D., Wheatley, P. J., et al. 2017, A&A, 599, L3
Caballero-Lopez, R. A., Engelbrecht, N. E., & Richardson, J. D. 2019, ApJ, 883, 73
Caballero-Lopez, R. A., & Moraal, H. 2004, JGRA, 109, A01101
Cliver, E. W., Schrijver, C. J., Shibata, K., & Usoskin, I. G. 2022, LRSP, 19, 2
Crutzen, P. J. 1970, QJRMS, 96, 320
Desorgher, L., Flückiger, E. O., & Gurtner, M. 2006, 36th COSPAR Scientific Assembly, 2361
Engelbrecht, N. E., & Di Felice, V. 2020, PhRvD, 102, 103007
Engelbrecht, N. E., Effenberger, F., Florinski, V., et al. 2022, SSRv, 218, 33
Engelbrecht, N. E., & Moloto, K. D. 2021, ApJ, 908, 167
Fraschetti, F., Drake, J. J., Alvarado-Gómez, J. D., et al. 2019, ApJ, 874, 21
Froning, C. S., France, K., Loyd, R. O. P., et al. 2018, AAS Meeting, 231, 111.05
Funke, B., Baumgaertner, A., Calisto, M., et al. 2011, ACP, 11, 9089
Garraffo, C., Drake, J. J., Cohen, O., Alvarado-Gómez, J. D., & Moschou, S. P. 2017, ApJL, 843, L33
Glazier, A. L., Howard, W. S., Corbett, H., et al. 2020, ApJ, 900, 27
Gleeson, L. J., & Axford, W. I. 1968, ApJ, 154, 1011
Greene, T. P., Bell, T. J., Ducrot, E., et al. 2023, Natur, 618, 39
Grenfell, J. L., Gebauer, S., Godolt, M., et al. 2013, AsBio, 13, 415
Grenfell, J. L., Grießmeier, J. M., von Paris, P., et al. 2012, AsBio, 12, 1109
Harbach, L. M., Moschou, S. P., Garraffo, C., et al. 2021, ApJ, 913, 130
Herbst, K., Baalmann, L. R., Bykov, A., et al. 2022b, SSRv, 218, 29
Herbst, K., Banjac, S., Atri, D., & Nordheim, T. A. 2020a, A&A, 633, A15
Herbst, K., Grenfell, J. L., Sinnhuber, M., et al. 2019, A&A, 631, A101
Herbst, K., Grenfell, J. L., Sinnhuber, M., & Wunderlich, F. 2022a, AN, 343, e10072
Herbst, K., Muscheler, R., & Heber, B. 2017, JGRA, 122, 23
Herbst, K., Scherer, K., Ferreira, S. E. S., et al. 2020b, ApJL, 897, L27
Hill, M. L., Bott, K., Dalba, P. A., et al. 2023, AJ, 165, 34
Ih, J., Kempton, E. M. R., Whittaker, E. A., & Lessard, M. 2023, ApJL, 952, L4
Jackman, C., DeLand, M., Labow, G., et al. 2005, AdSpR, 35, 445
Jackman, C., Marsh, D., Vitt, F., et al. 2011, ACP, 11, 6153
Jackman, C. H., Fleming, E. L., & Vitt, F. M. 2000, JGRD, 105, 11659
Jackman, C. H., McPeters, R. D., Labow, G. J., et al. 2001, GeoRL, 28, 2883
Kane, S. R. 2018, ApJL, 861, L21
Kasting, J. F., Whitmire, D. P., & Reynolds, R. T. 1993, Icar, 101, 108
Krissansen-Totton, J. 2023, ApJL, 951, L39

Lary, D. J. 1997, JGR, 102, 21515
Light, J., Ferreira, S. E. S., Engelbrecht, N. E., Scherer, K., & Herbst, K. 2022, MNRAS, 516, 3284
Lim, O., Benneke, B., Doyon, R., et al. 2023, ApJL, 955, L22
Lincowski, A. P., Meadows, V. S., Zieba, S., et al. 2023, ApJL, 955, L7
Luger, R., Sestovic, M., Kruse, E., et al. 2017, NatAs, 1, 0129
Matthaeus, W. H., Qin, G., Bieber, J. W., & Zank, G. P. 2003, ApJL, 590, L53
Matthes, K., Funke, B., Andersson, M. E., et al. 2017, GMD, 10, 2247
Mayor, M., & Queloz, D. 1995, Natur, 378, 355
McNair, A. 1981, J. Labelled Compd. Radiopharm., 18, 1398
Mekhaldi, F., Muscheler, R., Adolphi, F., et al. 2015, NatCo, 6, 8611
Mesquita, A. L., Rodgers-Lee, D., & Vidotto, A. A. 2021, MNRAS, 505, 1817
Mesquita, A. L., Rodgers-Lee, D., Vidotto, A. A., & Kavanagh, R. D. 2022, MNRAS, 515, 1218
Mikal-Evans, T. 2022, MNRAS, 510, 980
Miyake, F., Nagaya, K., Masuda, K., & Nakamura, T. 2012, Natur, 486, 240
Mollière, P., Wardenier, J. P., van Boekel, R., et al. 2019, A&A, 627, A67
Moloto, K. D., Engelbrecht, N. E., Strauss, R. D., Moeketsi, D. M., & van den Berg, J. P. 2019, AdSpR, 63, 626
Moraal, H. 2013, SSRv, 176, 299
Neichel, B., Mouillet, D., Gendron, E., et al. 2018, SF2A-2018: Proc. of the Annual Meeting of the French Society of Astronomy and Astrophysics, ed. P. Di Matteo, F. Billebaud, F. Herpin et al.
Nicolet, M. 1965, JGR, 70, 691
Nicolet, M. 1975, P&SS, 23, 637
Nieder, H., Winkler, H., Marsh, D. R., & Sinnhuber, M. 2014, JGRA, 119, 2137
Papaioannou, A., Herbst, K., Ramm, T., et al. 2023, A&A, 671, A66
Parker, E. N. 1958, ApJ, 128, 664
Parker, E. N. 1965, P&SS, 13, 9
Quanz, S. P., Ottiger, M., Fontanet, E., et al. 2022, A&A, 664, A21
Rodgers-Lee, D., Taylor, A. M., Vidotto, A. A., & Downes, T. P. 2021, MNRAS, 504, 1519
Rühm, W., Azizova, T., Bouffler, S., et al. 2018, JRadR, 59, ii1
Scheucher, M., Grenfell, J., Wunderlich, F., et al. 2018, ApJ, 863, 6
Scheucher, M., Herbst, K., Schmidt, V., et al. 2020a, ApJ, 893, 12
Scheucher, M., Wunderlich, F., Grenfell, J. L., et al. 2020b, ApJ, 898, 44
Schreier, F., Gimeno García, S., Hedelt, P., et al. 2014, JQSRT, 137, 29
Schreier, F., Gimeno García, S., Vasquez, M., & Xu, J. 2015, JQSRT, 164, 147
Schreier, F., Milz, M., Buehler, S., & von Clarmann, T. 2018a, JQSRT, 211, 64
Schreier, F., Städt, S., Hedelt, P., & Godolt, M. 2018b, MolAs, 11, 1
Segura, A., Kasting, J. F., Meadows, V., et al. 2005, AsBio, 5, 706
Shalchi, A. 2009, APh, 31, 237
Shen, Z. N., Qin, G., Zuo, P., & Wei, F. 2019, ApJ, 887, 132
Sinnhuber, M., & Funke, B. 2020, in The Dynamic Loss of Earth's Radiation Belts: From Loss in the Magnetosphere to Particle Precipitation in the Atmosphere, ed. A. N. Jaynes & M. E. Usanova (Amsterdam: Elsevier), 279
Sinnhuber, M., Nieder, H., & Wieters, N. 2012, SGeo, 33, 1281
Solomon, S., Rusch, D., Gerard, J. C., Reid, G., & Crutzen, P. 1981, P&SS, 29, 885
Stone, E. C., Cummings, A. C., McDonald, F. B., et al. 2013, Sci, 341, 150
Strauss, R. D. T., & Effenberger, F. 2017, SSRv, 212, 151
Swider, W., & Keneshea, T. J. 1973, P&SS, 21, 1969
Tabataba-Vakili, F., Grenfell, J. L., Grießmeier, J. M., & Rauer, H. 2016, A&A, 585, A96
Tian, F., France, K., Linsky, J. L., Mauas, P. J. D., & Vieytes, M. C. 2014, E&PSL, 385, 22
Van Grootel, V., Fernandes, C. S., Gillon, M., et al. 2018, ApJ, 853, 30
Vida, K., Kővári, Z., Pál, A., Oláh, K., & Kriskovics, L. 2017, ApJ, 841, 124
Webber, W. R., Cummings, A. C., McDonald, F. B., et al. 2008, JGR, 113, A10108
Wedlund, C. S., Gronoff, G., Lilensten, J., Ménager, H., & Barthélemy, M. 2011, AnG, 29, 187
Wheatley, P. J., Louden, T., Bourrier, V., Ehrenreich, D., & Gillon, M. 2017, MNRAS, 465, L74
Wilson, D., Froning, C. S., France, K., et al. 2019, AAS Meeting, 233, 205.05
Wilson, D. J., Froning, C. S., Duvvuri, G. M., et al. 2021, ApJ, 911, 18
Winkler, H., Kazeminejad, S., Sinnhuber, M., Kallenrode, M. B., & Notholt, J. 2009, JGRD, 114, D00I03
Wunderlich, F., Scheucher, M., Godolt, M., et al. 2020, ApJ, 901, 126
Zhang, Z., Zhou, Y., Rackham, B. V., & Apai, D. 2018, AJ, 156, 178
Zieba, S., Kreidberg, L., Ducrot, E., et al. 2023, Natur, 620, 746